Engineering water splitting sites in three-dimensional flower-like Co-Ni-P/MoS$_2$ heterostructural hybrid spheres for accelerating electrocatalytic oxygen and hydrogen evolution

Jiehua Bao [a], Yuming Zhou *[a,c], Yiwei Zhang *[a], Xiaoli Sheng [a], Yanyun Wang [a], Shuang Liang [b], Chang Guo [a,c], Wei Yang [a,d], Tao Zhuang [a,e,f], Yingjie Hu *[g].

[a] Jiangsu Optoelectronic Functional Materials and Engineering Laboratory, School of Chemistry and Chemical Engineering, Southeast University, Nanjing 211189, P.R. China.

[b] School of Chemical and Biomolecular Engineering, Georgia Institute of Technology, Atlanta, GA 30332, USA.

[c] Nanjing Guoxing Biotechnology Research Institute Co. LTD, Nanjing 211300, P. R. China.

[d] Sunrise Packaging Material (Jiangyin) Co., Ltd, Jiangyin, 214411, P. R. China.

[e] Key Laboratory of Rubber-Plastics, Ministry of Education/Shandong Provincial Key Laboratory of Rubber-plastics, Qingdao University of Science & Technology, Qingdao, 266042, P.R. China.

[f] Shandong Yanggu Huatai Chemical Co., Ltd., Liaocheng 252300, P.R. China.

[g] Key Laboratory of Advanced Functional Materials of Nanjing, Nanjing Xiaozhuang University, Nanjing 211171, P.R. China.

Corresponding Authors

E-mail: ymzhou@seu.edu.cn (Y.M. Zhou), zhangchem@seu.edu.cn (Y.W. Zhang), huyj113@qq.com (Y.J. Hu)

EXPERIMENTAL SECTION

Materials.

cobalt nitrate hexahydrate ($Co(NO_3)_2 \cdot 6H_2O$), nickel nitrate hexahydrate ($Ni(NO_3)_2 \cdot 6H_2O$), 2-methylimidazole ($C_4H_6N_2$), ammonium molybdate tetrahydrate (($NH_4)_6Mo_7O_{24} \cdot 4H_2O$), sulfocarbamide ($CH_4N_2S$), methanol ($CH_3OH$), commercial Pt/C (20%), and commercial RuO_2 were purchased from Sigma-Aldrich. All chemicals were of analytical grade and used without further purification. De-ionized water was obtained by reversed osmosis followed by ion-exchange and filtration.

Synthesis of 3D flower-like Co-Ni MOF spheres.

For the typical synthesis of Co-Ni MOF, Firstly, 0.9 g $Co(NO_3)_2 \cdot 6H_2O$ and 0.3 g $Ni(NO_3)_2 \cdot 6H_2O$ were dissolved in 30 mL CH_3OH, labeled as solution A. Then, 0.2 g 2-methylimidazole was dissolved in 10 mL CH_3OH, labeled as solution B. Finally, the solution A was added to the solution B and magnetically stirred for 30 min. The well-mixed solution was allowed to stand at room temperature for 24 hours. The Co-Ni MOF was collected by centrifugation and washed with CH_3OH and H_2O for several times and dried at 80℃ for 12 h.

Synthesis of 3D flower-like Co-Ni-P spheres.

Typically, 100 mg flower-like Co-Ni MOF spheres was firstly calcined at 300℃ for 2 h in air at a heating rate of 2℃ min^{-1}. The calcined product and 5 g NaH_2PO_2 were placed in two separate locations in a tube furnace, and NaH_2PO_2 was located on the upstream side of the furnace. The solid was calcined at 300℃ for 5 h in N_2 at a heating rate of 2℃ min^{-1}. The flower-like Co-Ni-P spheres was collected after cooling to room temperature under N_2.

Synthesis of 3D flower-like Co-Ni-P/MoS$_2$ heterostructures hybrid spheres.

In a typical preparation, 58 mg ($NH_4)_6Mo_7O_{24} \cdot 4H_2O$ and 0.91 g sulfocarbamide were dissolved in 70 ml H_2O. Then, 50 mg flower-like Co-Ni-P spheres were added, and this mixture was kept with magnetic stirring for 1h. After this period, the mixture was transferred to a Teflon-lined stainless steel autoclave at 200℃ for 10 h. The 3D flower-like Co-Ni-P/MoS$_2$ heterostructures hybrid spheres was collected by centrifugation and washed with CH_3OH and H_2O for several times and dried at 80℃ for 12 h.

For comparison, the MoS_2 was prepared using the similar method without addition of flower-like Co-Ni-P spheres.

Characterization.

Field emission scanning electron microscopy (SEM) images were obtained on a FEI Inspect F50 instrument. Transmission electron microscopy (TEM) and EDS elemental mapping analyses were conducted on JEOL JEM-2010F instruments. The X-ray diffraction (XRD) patterns of the catalyst samples were recorded on a Rigaku Ultima IV diffractometer using Cu Ka radiation ($\lambda = 0.15418$ nm) with a scanning speed of $4° \cdot min^{-1}$ and the various crystalline phases identification was based on the Joint Committee on Powder Diffraction Standards (JCPDSs). Nitrogen physisorption were obtained at -196 °C on the Micromeritics ASAP 2020 system. Prior to the measurement, the sample was degassed at 200 °C for 3 h under vacuum to remove adsorbed gases and moisture. X-ray photoelectron spectroscopy (XPS) were measured using an ESCALAB MKII X-ray photo-electron spectrometer with Al Ka radiation.

Electrochemical measurements.

Electrochemical properties of the samples were evaluated in a three-electrode system with an electrochemical workstation (CH Instruments 660E, Shanghai Chenhua) at 298K. The glassy carbon disk (GCE 4.0 mm in diameter) coated by catalysts films, graphite rod and saturated calomel electrode were used as the working electrode, counter electrode and reference electrode, respectively. The optimal catalyst loading on the glassy carbon disk was around 0.4 mg cm^{-2}. All the potentials were determined with respect to RHE using the equation: $E_{RHE} = E_{SCE} + 0.241$ V $+ 0.0591$ pH. The Tafel slopes were calculated by fitting to the Tafel equation: $\eta = b \log j + c$, where b is the Tafel slope, j is the current density and c is the intercept relative to j_0. TOF of the catalysts were calculated according to the following equation: $TOF = I / (2F \cdot n)$, where I is the current (in amperes), F is the Faraday constant (96,485.3 C·mol^{-1}), and n is the number of moles of the active catalyst.

DFT calculations.

In this work, the density functional theory (DFT) calculation was performed by the Cambridge serial total energy package (CASTEP) code, in which a plane wave basis set was used. The exchange and

correlation interactions were modeled using the generalized gradient approximation (GGA) and the Perdew-Burke-Ernzerhof (PBE) functional. The Vanderbilt ultrasoft pseudopotential was used with a cutoff energy of 340 eV. Geometric convergence tolerances were set for maximum force of 0.03 eV/A°, maximum energy change of 10^{-5} eV/atom, maximum displacement of 0.001 A° and maximum stress of 0.5 GPa. Density mixing electronic minimisation was implemented and the self-consistent field (SCF) tolerance was set to ''fine'' with high accuracy of 10^{-6} eV/atom for energy convergence. The Gibbs free energy change (ΔG_{H*}) shows the following express: $\Delta G_{H*} = \Delta E_{H*} + \Delta E_{ZPE} - T\Delta S$, where ΔE_{H*}, ΔE_{ZPE} and ΔS are the adsorption energy of atomic hydrogen on the given surface, zero point energy correction and entropy change of H* adsorption, respectively. The zero point energy correction is estimated by the equation $\Delta E_{ZPE} = E_{ZPE}(H^*)$ 1/2 $E_{ZPE}(H_2)$, where $E_{ZPE}(H^*)$ and $E_{ZPE}(H_2)$ are calculated by vibration frequency calculation. At 1 bar and 300 K, $T\Delta S$ is approximately -0.2 eV. The value of ΔE_{H*} is calculated as $\Delta E_{H*} = E_{tot} - E_{sub} - 1/2E_{H2}$, where E_{tot} and E_{sub} are the energies of H absorbed systems and the clean given surface, respectively, and E_{H2} is the energy of molecular H_2 in the gas phase. The following mechanism of oxygen evolution reaction was adopted. $H_2O + * \rightarrow *OH + H^+ + e^-$, $*OH \rightarrow *O + H^+ + e^-$, $H_2O(l) + *O \rightarrow *OOH + H^+ + e^-$, $*OOH \rightarrow * + O_2 + H^+ + e^-$. The ''*'' represented the active site when OER occurred. The ''*OH'', ''*O'', ''*OOH'' represented the intermediate species adsorbed on the active sites. In order to evaluate OER activity, we calculated the free energy ($\Delta G_1 \sim \Delta G_4$) using the computational standard hydrogen electrode model. The free energy calculation could be obtained as follows: $\Delta G_1 = E(*OH) - E(*) - E(H_2O) + 1/2E_{H2} - eU + \Delta ZPE - T\Delta S + K_B TLn10 \cdot pH$, $\Delta G_2 = E(*O) + 1/2E(H_2) - E(*OH) - eU + \Delta ZPE - T\Delta S + K_B TLn10 \cdot pH$, $\Delta G_3 = E(*OOH) + 1/2E(H_2) - E(H_2O) - E(*O) - eU + \Delta ZPE - T\Delta S + K_B TLn10 \cdot pH$, $\Delta G_4 = 4.92 - \Delta G_1 - \Delta G_2 - \Delta G_3$. It should be noted that E(*), E(*OH), E(*O), E(*OOH) represented the total energy of the coordinate species adsorbed in the active sites which calculated by DFT. The energy of $H^+ + e^-$ was substituted by $1/2E(H_2)$ under pH = 0, p = 1 atm, T = 298 K conditions. ZeroPoint Energy (ZPE) and entropy (TS) change for gas molecules (H_2, O_2, H_2O) could be found, based on our calculation and confirmed by previous reports. -eU represented the free energy changes for one electron transfer where U was electrode potential respect to the standard hydrogen

electrode. For pH $\neq$ 0, pH effected on free energy could be defined as $-K_B T \mathrm{Ln}10 \cdot pH$, where K_B was Boltzman constant. ΔG_4 was calculated by $4.92 - \Delta G_1 - \Delta G_2 - \Delta G_3$ to avoid calculating the O_2 adsorption and desorption. It was known that the DFT calculation might not accurately describe the free energy of O_2 molecule in the gas phase and hence we used H_2O and H_2 as reference and from there we extracted the free energy of O_2 through the reaction $O_2 + 4(H^+ + e^-) \rightarrow 2H_2O$. The equilibrium potential for this reaction was 1.23 V and since it was a four electrons transfer reaction, the full energy was $4 \times 1.23 = 4.92$ eV. This analysis was based on the scheme developed by Norskov's group. The overpotential of OER in this mechanism was defined as $\eta_{OER} = \max(\Delta G_{OER}/e) - 1.23$ V.

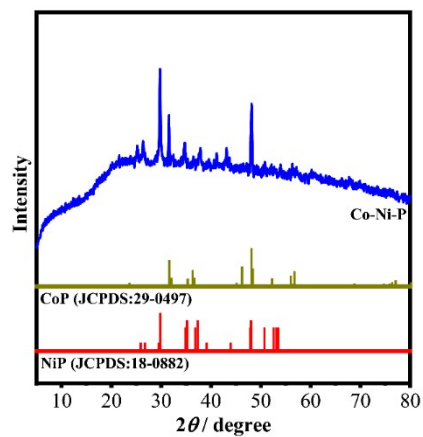# Supplementary figures
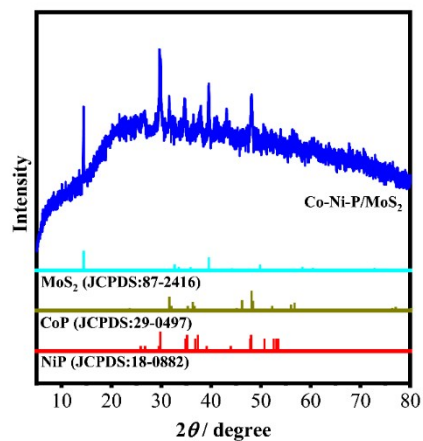

Fig. S1 XRD patterns of the Co-Ni-P.

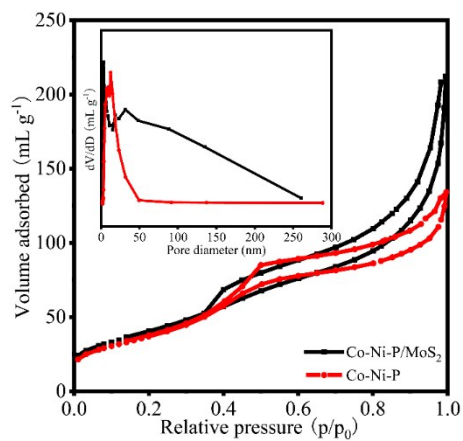**Fig. S2** XRD patterns of the Co-Ni-P/MoS$_2$.

Fig. S3 N$_2$ adsorption-desorption isotherms and pore-size distribution curves of the Co-Ni-P/MoS$_2$ and Co-Ni-P.
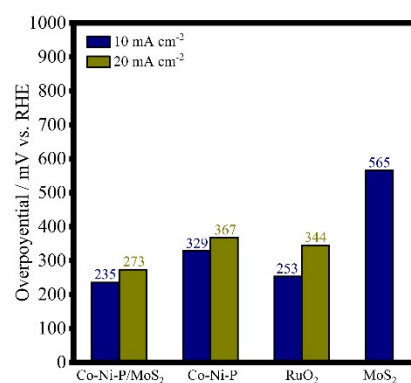
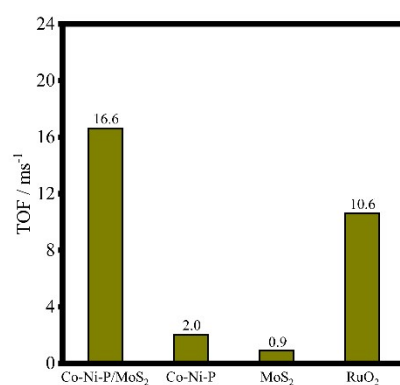**Fig. S4** Required overpotentials derived from OER polarization curves at different current densities,

Fig. S5 Comparison of TOF at overpotentials of 200mV for Co-Ni-P/MoS$_2$, Co-Ni-P, MoS$_2$, and RuO$_2$.
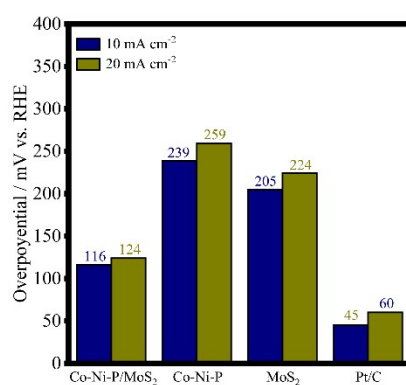

Fig. S6 Required overpotentials derived from HER polarization curves at different current densities,
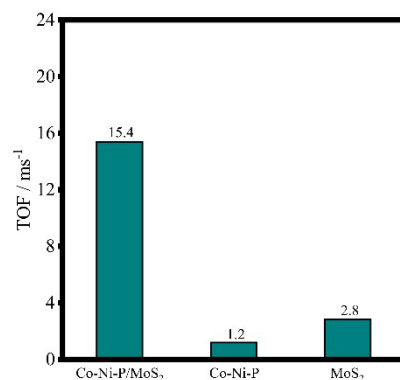
Fig. S7 Comparison of TOF at overpotentials of 100mV for Co-Ni-P/MoS$_2$, Co-Ni-P, and MoS$_2$.
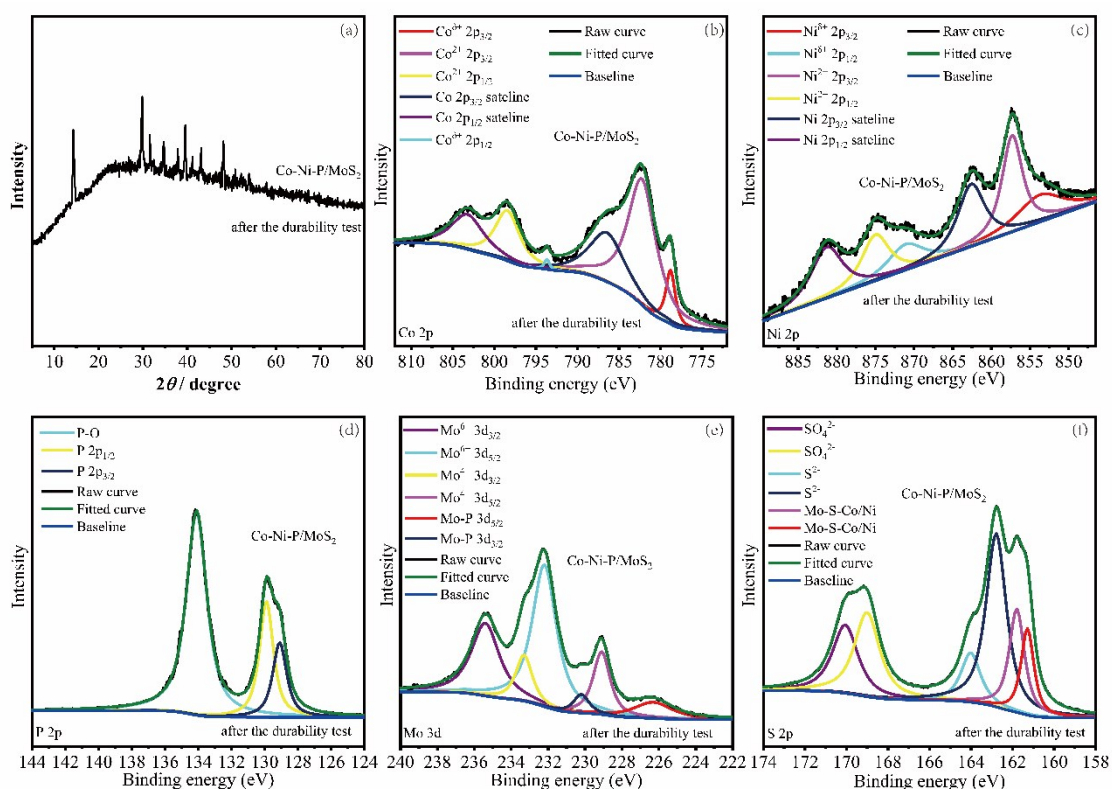

Fig. S8 (a) XRD patterns of Co-Ni-P/MoS$_2$ after stability tests. High-resolution XPS spectra of the Co-Ni-P/MoS$_2$ after stability tests: (b) Co 2p, (c) Ni 2p, (d) P 2p, (e) Mo 3d, and (f) S 2p.
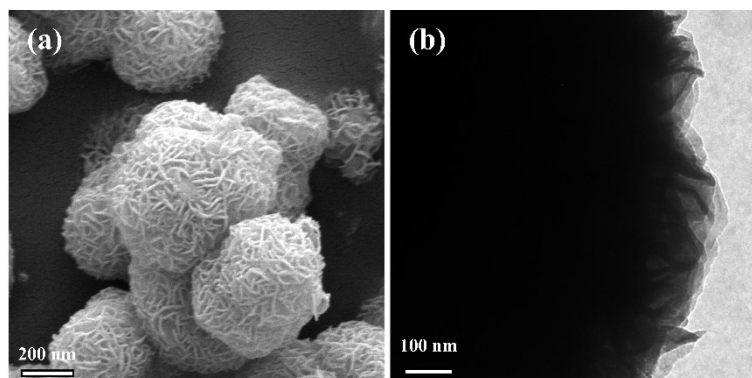
Fig. S9 (a) FESEM and (b) TEM images of Co-Ni-P/MoS$_2$ after stability tests.
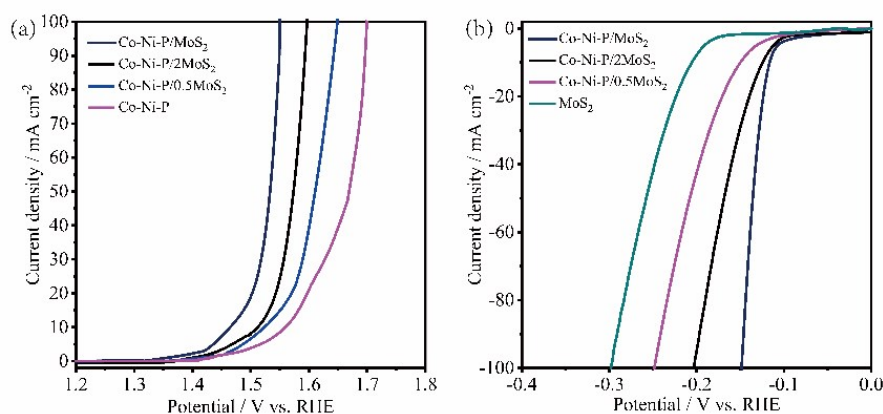
Fig. S10 (a) OER polarization curves of the Co-Ni-P/MoS$_2$, Co-Ni-P/2MoS$_2$, Co-Ni-P/0.5MoS$_2$, and Co-Ni-P. (b) HER polarization curves of the Co-Ni-P/MoS$_2$, Co-Ni-P/2MoS$_2$, Co-Ni-P/0.5MoS$_2$, and MoS$_2$.

Fig. S11. (a) Schematic illustration of water activation, H* intermediate formation, and hydrogen generation processes on MoS$_2$. (b) Schematic illustration of water activation, *OH/O*/*OOH generation, and oxygen generation processes on Co-Ni-P.

Fig. S12 CV curves of Co-Ni-P/MoS$_2$ in the double layer region at scan rates of 5, 10, 15, 20, 25 and 30 mV s^{-1} in 1.0 M KOH

Supplementary tables

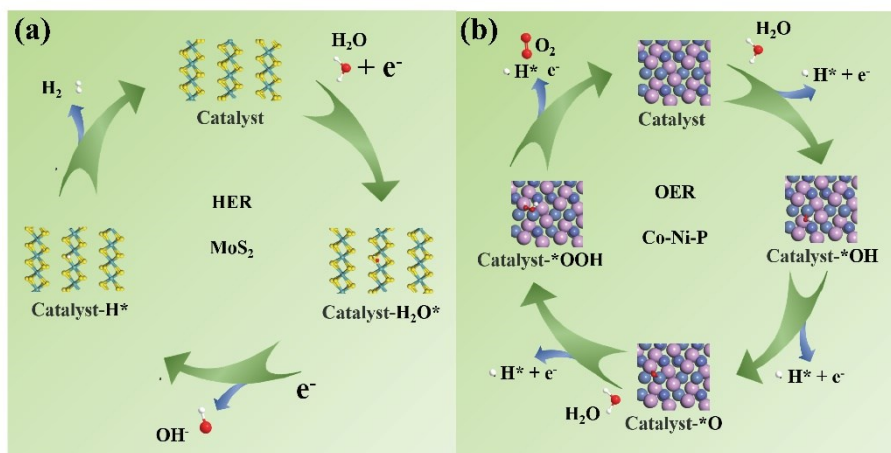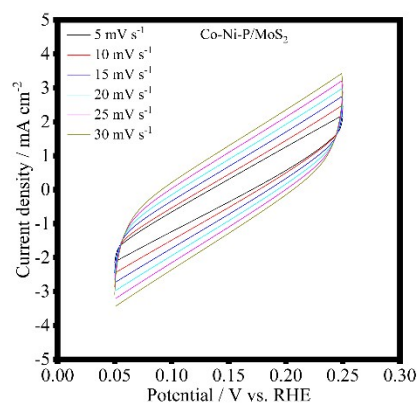Table S1 Comparison of the OER performances of representative electrocatalysts in alkaline electrolyte.

Catalyst	Electrolyte	Mass loading (mg cm^{-2})	Tafel slope (mV dec^{-1})	Overpotential at 10 mA cm^{-2} (mV)	Reference
Co-Ni-P/MoS$_2$	1 M KOH	0.4	71	235	This work
Co-Ni-P	1 M KOH	0.4	95	329	This work
Ni-Co-P nanosheets	1 M KOH	2	88	270	[1]
NiCoP/C	1 M KOH	0.25	96	330	[2]
Co-Ni-P	1 M KOH	/	98	340	[3]
Co1Ni4P	1 M KOH	0.19	94	245	[4]
Co-MoS$_2$/BCCF-21	1 M KOH	2	85	260	[5]
MoS$_2$/NiS$_2$-3	1 M KOH	/	91.7	278	[6]
Co/CoP-5	1 M KOH	0.88	79.5	283	[7]
PO-Ni/Ni-N-CNFs	1 M KOH	8	113.1	420	[8]
NiCoP NWAs/NF	1 M KOH	8	116	/	[9]
MoS$_2$/Ni$_3$S$_2$	1 M KOH	/	88	218	[10]
Co-Mo$_2$N	1 M KOH	0.7077	90	302	[11]
CoOx-MoC/NC-2	1 M KOH	0.65	89.8	330	[12]

Table S2 Comparison of the HER performances of representative electrocatalysts in alkaline electrolyte.

Catalyst	Electrolyte	Mass loading (mg cm^{-2})	Tafel slope (mV dec^{-1})	Overpotential at 10 mA cm^{-2} (mV)	Reference
Co-Ni-P/MoS$_2$	1 M KOH	0.4	41	116	This work
MoS$_2$	1 M KOH	0.4	61	205	This work
Ni-Co-P nanosheets	1 M KOH	2	53	107	[1]
Co-Ni-P	1 M KOH	/	81	103	[3]
Co4Ni1P	1 M KOH	0.19	52	129	[4]
Co-MoS$_2$/BCCF-21	1 M KOH	2	52	48	[5]
MoS$_2$/NiS$_2$-3	1 M KOH	/	50.1	62	[6]
Co/CoP-5	1 M KOH	0.88	73.8	193	[7]
PO-Ni/Ni-N-CNFs	1 M KOH	8	97.42	313	[8]
NiCoP NWAs/NF	1 M KOH	8	54	104	[9]
MoS$_2$/Ni$_3$S$_2$	1 M KOH	/	83	110	[10]
Co-Mo$_2$N	1 M KOH	0.7077	47	76	[11]
Co$_3$O$_4$/MoS$_2$	1 M KOH	2	128	205	[13]
Ni(OH)$_2$/MoS$_2$@CC	1 M KOH	/	60	80	[14]

Table S3 Comparison of overall water splitting performances of representative electrocatalysts.

Catalyst	Electrolyte	Potential at 10 mA cm^{-2} (V)	Reference
Co-Ni-P/MoS$_2$	1 M KOH	1.53	This work
Ni-Co-P nanosheets	1 M KOH	1.75	[1]
Co-Ni-P	1 M KOH	1.65	[3]
Co4Ni1P	1 M KOH	1.59	[4]
MoS$_2$/NiS$_2$-3	1 M KOH	1.59	[6]
PO-Ni/Ni-N-CNFs	1 M KOH	1.69	[8]
MoS$_2$/Ni$_3$S$_2$	1 M KOH	1.56	[10]
Ni$_2$P nanowires	1 M KOH	1.63	[15]
EG/Co$_{0.85}$Se/NiFe LDH	1 M KOH	1.67	[16]
CoP	1 M KOH	1.65	[17]
NiCo$_2$O$_4$	1 M KOH	1.65	[18]
NiCo$_2$O$_4$/Ni$_2$P	1 M KOH	1.59	[19]
Ni$_5$P$_4$ films	1 M KOH	1.69	[20]

References

1. E. Hu, Y. Feng, J. Nai, D. Zhao, Y. Hu and X. W. Lou, *Energy Environ. Sci.*, 2018, **11**, 872-880.
2. P. He, X. Y. Yu and X. W. Lou, *Angew. Chem. Int. Ed.*, 2017, **56**, 3897-3900.
3. Y. Pei, Y. Yang, F. Zhang, P. Dong, R. Baines, Y. Ge, H. Chu, P. M. Ajayan, J. Shen and M. Ye, *ACS Appl. Mater. Interfaces*, 2017, **9**, 31887-31896.
4. L. Yan, L. Cao, P. Dai, X. Gu, D. Liu, L. Li, Y. Wang and X. Zhao, *Adv. Funct. Mater.*, 2017, **27**, 1703455.
5. Q. Xiong, Y. Wang, P. F. Liu, L. R. Zheng, G. Wang, H. G. Yang, P. K. Wong, H. Zhang and H. Zhao, *Adv. Mater.*, 2018, **30**, 1801450.
6. J. Lin, P. Wang, H. Wang, C. Li, X. Si, J. Qi, J. Cao, Z. Zhong, W. Fei and J. Feng, *Adv. Sci.*, 2019, **6**, 1900246.
7. Z. H. Xue, H. Su, Q. Y. Yu, B. Zhang, H. H. Wang, X. H. Li and J. S. Chen, *Adv. Energy Mater.*, 2017, **7**, 1602355.
8. Z. Y. Wu, W. B. Ji, B. C. Hu, H. W. Liang, X. X. Xu, Z. L. Yu, B. Y. Li and S. H. Yu, *Nano Energy*, 2018, **51**, 286-293.
9. J. Li, G. Wei, Y. Zhu, Y. Xi, X. Pan, Y. Ji, I. V. Zatovsky and W. Han, *J. Mater. Chem. A*, 2017, **5**, 14828-14837.
10. J. Zhang, T. Wang, D. Pohl, B. Rellinghaus, R. Dong, S. Liu, X. Zhuang and X. Feng, *Angew. Chem. Int. Ed.*, 2016, **55**, 6702-6707.
11. X. Shi, A. Wu, H. Yan, L. Zhang, C. Tian, L. Wang and H. Fu, *J. Mater. Chem. A*, 2018, **6**, 20100-20109.
12. T. Huang, Y. Chen and J.-M. Lee, *Small*, 2017, **13**, 1702753.
13. A. Muthurasu, V. Maruthapandian and H. Y. Kim, *Appl. Catal., B*, 2019, **248**, 202-210.
14. B. Zhang, J. Liu, J. Wang, Y. Ruan, X. Ji, K. Xu, C. Chen, H. Wan, L. Miao and J. Jiang, *Nano Energy*, 2017, **37**, 74-80.
15. L. A. Stern, L. Feng, F. Song and X. Hu, *Energy Environ. Sci.*, 2015, **8**, 2347-2351.
16. Y. Hou, M. R. Lohe, J. Zhang, S. Liu, X. Zhuang and X. Feng, *Energy Environ. Sci.*, 2016, **9**, 478-483.
17. T. Liu, L. Xie, J. Yang, R. Kong, G. Du, A. M. Asiri, X. Sun and L. Chen, *ChemElectroChem*, 2017, **4**, 1840-1845.
18. X. Gao, H. Zhang, Q. Li, X. Yu, Z. Hong, X. Zhang, C. Liang and Z. Lin, *Angew. Chem. Int. Ed.*, 2016, **55**, 6290-6294.
19. L. Wang, C. Gu, X. Ge, J. Zhang, H. Zhu and J. Tu, *Advanced Materials Interfaces*, 2017, **4**, 1700481.
20. M. Ledendecker, S. Krick Calderón, C. Papp, H.-P. Steinrück, M. Antonietti and M. Shalom, *Angew. Chem. Int. Ed.*, 2015, **54**, 12361-12365.